Pergamon

Int. J. Heat Mass Transfer. Vol. 38, No. 11, pp. 2057–2073, 1995

0017-9310/95 $9.50+0.00

0017-9310(94)00315-7

Simulation of interfacial instabilities during solidification—I. Conduction and capillarity effects

H. S. UDAYKUMAR and W. SHYY†

Department of Aerospace Engineering, Mechanics and Engineering Science, University of Florida, Gainesville, FL 32611, U.S.A.

(*Received* 25 *February* 1994 *and in final form* 15 *September* 1994)

Abstract—A combined Eulerian–Lagrangian numerical method is developed for simulating deformed interfaces arising in the solidification of pure materials. The interface tracking procedure employs marker particles and is the Lagrangian component of the calculation. The field equations are solved in a fixed Eulerian framework, so that the interface passes through the grid layout. Information from the explicitly tracked interface is used to apply boundary conditions at the exact interface location in each computational cell, in contrast with other Eulerian schemes. Consistent with the the established theory, in the absence of surface tension, the present simulations result in different types of behavior such as tip-splitting and cusp formation. For low surface tensions, due to the lack of physical length scales, the solutions are qualitatively affected by grid resolution with no unique solution available. In contrast, with substantial surface tension values the initial perturbation grows to form long fingers. The finger shapes reflect the stabilizing effects of capillarity. Unique solutions can be reached with nonzero surface tension.

1. INTRODUCTION

Numerous physical systems, in natural as well as man made environments, contain interfaces demarcating regions of distinct physico-chemical properties [1, 2]. The interfaces in these systems may be idealized as discontinuities across which compositions, phases, material properties and flow features change rapidly. Under certain conditions, usually characterized by one or more control parameters, these interfaces experience instabilities such as in viscous fingering [3–5], solidification [1, 2, 6, 7], and other phenomena [8–11]. Typically, a cascade of interfacial instabilities leads to the formation of patterns and morphological structures reflecting the interaction of the microscopic and macroscopic properties of the system. For example, the formation of deep cells in the growth of impure (i.e. multi-component) materials has considerable significance in regard to the resulting compositional inhomogeneities (*segregation*), which may affect the performance and properties of doped semiconductors and the structural integrity of alloy materials [6, 7].

Conventionally, the onset and linear growth of disturbances in the above mentioned phenomena have been investigated using linear stability theory. Weakly nonlinear analyses in extension of the onset behavior have also been performed [12]. However, far from onset, the interfaces undergo successive instabilities of various types and in some systems the final observed pattern may deviate significantly from that predicted by linear stability analyses. In other cases, the instability may be triggered by large amplitude disturbances and such subcritical phenomena are obviously not accessible to linear stability considerations. The mechanisms by which the nonlinear phenomena induce reorganizations and coherent patterns in unstable systems are not therefore clarified by analyses restricted to small perturbations. Thus, sufficient motivation exists for developing general investigative capabilities in order to study the above mentioned phenomena in their highly non-linear stages. This regime is most accessible to laboratory and computational experiments. The effort presented herein is devoted to developing a tool for computational study of the instability of interfaces far into the nonlinear growth stages.

We choose, as our model system, the growth of crystals of pure materials from the melt. The mechanisms of instability and various aspects of pattern selection and transport phenomena have been thoroughly investigated over the years and the literature abounds in refs. [12–16]. Thus, we detail only such features of the morphological evolution as are necessary to provide a motivation for the numerical procedure developed here.

Consider the typical crystal growth situation depicted in Fig. 1(a). Let the wall on the liquid side be maintained at a temperature T_l such that $T_l < T_m$, the melting temperature of the material, i.e. the melt is *undercooled*. The interface between solid and liquid corresponds approximately to the isotherm $T(x, t) = T_m$. Thus, the protrusion of the bump into

† Author to whom correspondence should be addressed.

NOMENCLATURE

A	area
C_p	specific heat at constant pressure
d_o	capillary length scale
(i,j)	indices
k	thermal conductivity
l_T	thermal boundary layer thickness
L	latent heat of fusion
$\mathbf{n}$	non-dimensional normal vector
$\mathbf{N}$	dimensional normal vector
R	radius of curvature
S	interface position
St	Stefan number
t	non-dimensional time
T	dimensional temperature
V	front velocity
(x,y)	non-dimensional coordinates
(X,Y)	dimensional coordinates.

Greek symbols

α	thermal diffusivity
ξ	a constant, equation (19)
Δ	undercooling
$\varepsilon_1, \varepsilon_2$	scaling constants
γ	surface tension
κ	surface curvature
ψ	arclength
λ	a constant, equation (23)
λ_c	morphological length scale
v	non-dimensional velocity of front
ϕ	angle measured from the horizontal
ρ	density
τ	time scale
θ	non-dimensional temperature
χ	non-dimensional domain size.

Subscripts

i	interface
l	liquid
m	melting point value
n	normal direction
o	initial condition
s	solid
t	tip value.

Superscripts

*	non-dimensional value.

the liquid leads to a clustering of the isotherms in the vicinity of the tip, implying a higher temperature gradient there. The bump is thereby induced to lose latent heat more rapidly in comparison with the other regions of the interface, which causes the disturbance to run away to form a finger. For growth of an unstable front in the pure material system, the available exact solutions were obtained by Ivantsov [12, 14–16] in the form of paraboloids of revolution. These solutions have the property that, for given values of undercooling, they represent a continuous family of solutions, and specify only the combination $R_t\ V_t$, where R_t is the tip radius and V_t is the tip velocity of the paraboloid. However, it is observed that the tip radius and velocity assume unique values as functions of undercooling in real growth systems [14]. Thus, a selection mechanism is missing from the Ivantsov model, which fails to take account of an important physical ingredient, namely surface tension (γ). Surface tension appears as the controlling factor, to select a discrete set of solutions from the continuum of solutions [1]. The stabilization of the interface is accomplished by surface tension by modifying the interfacial temperature, which no longer corresponds to the T_m isotherm. In particular, in two dimensions the Gibbs–Thomson condition for the interfacial temperature reads

$$T_i = T_m\left(1-\left(\gamma(\phi)+\frac{\partial^2\gamma(\phi)}{\partial\phi^2}\right)\kappa/L\right) \qquad (1)$$

where $\gamma(\phi)$ is the surface tension, ϕ is the angle between the normal and the x-axis, L is the latent heat of fusion and κ is the interfacial curvature [7]. The dependence on orientation, i.e. the surface tension anisotropy, is a reflection of the underlying solid lattice structure. From equation (1), it is evident that surface tension depresses the temperature at the tip, reducing the effective undercooling there, and providing a stabilizing effect. In essence, surface tension, reflecting the existence of a critical nucleation radius, provides a short wavelength cutoff for the instabilities. The selected dendrite tip is highly sensitive to noise and behaves like an amplifier [17]. Thus, the final shape of the crystal is not usually represented by a smooth paraboloid, but a highly branched structure, with successive instabilities ensuing on sidebranches at different scales [14].

Recently, much interest has also been generated in regard to the effects of convection, natural and forced, on the macroscopic and microscopic interfacial characteristics [16, 18, 19], motivated by low-gravity crystal growth experiments [20], and the possibility of controlling microstructure using forced convection [21]. Convection further complicates the issues by bringing in length and time scales disparate from the interfacial instability phenomena, and breaking symmetry. While phenomena at the macroscopic scale have been well investigated [16], at the morphological scales studies thus far have only been of an idealized nature. These effects will be studied in the future, by extending the numerical methods presented in this work.

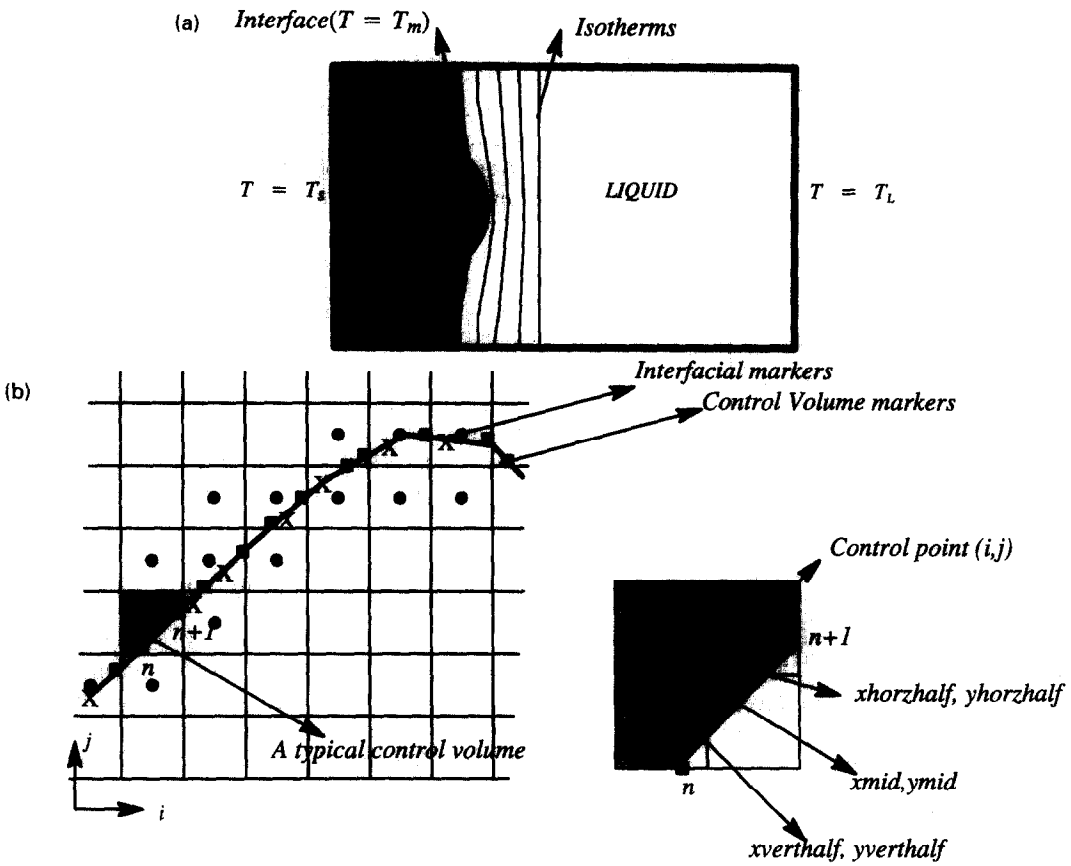

Fig. 1. Illustration of physical and computational arrangements involving irregular interfaces. (a) Typical crystal growth situation involving an undercooled melt showing clustering of isotherms in front of the bump. (b) Arrangement of interfacial and control volume markers and definition of a typical control volume. n and $n+1$ are indices of the control volume markers.

In our previous effort [22] we developed an interface tracking procedure that can handle highly deformed interfaces and surmounts the conventionally accepted difficulty in handling topological changes. In the context of Lagrangian methods, Glimm *et al.* [23] have applied similar approaches to perform merger/breakup operations for the viscous fingering problem. In the approach presented here, we seek to exploit the knowledge of exact interfacial location in formulating conservative and consistent differencing schemes via the control volume formulation. This is the advantage that the surface-tracking method [22–33] affords in contrast to volume-tracking schemes [34–39]. Performing the calculations on a stationary Cartesian grid yields conveniently to a control volume formulation [40, 41] and iterative line solvers. Thus far, Cartesian grid methods have either been restricted to volume-tracking procedures or have failed to exploit the explicit specification of the interface position. In other cases, such as in [29, 42], particle tracking has been employed. However, in each case the exact boundary conditions have not been rigorously applied in the finite difference formulation. The concern in these works was not directed as in our case, on conservation across the interface. Cartesian grid solutions for arbitrarily shaped bodies which pass through the grid, have been advanced recently for inviscid flow over stationary obstacles [43, 44]. While more detailed assessment is needed, the use of fixed grids with cell partition technique to accommodate the irregular internal boundary appears promising.

In the present problem, the interface grows in perimeter in the course of the instability. Interfaces may merge or fragment. The solution procedure is therefore required to follow the evolution of an interface under these circumstances. The behavior of the interface is very sensitive to the intricate details of the boundary conditions applied at the interface. In particular, as we demonstrate later, surface tension is a delicate mechanism but has a significant effect on the finally attained shape. Since the surface tension multiplies the curvature of the interface, the numerical scheme is required to compute the interface shape and the first and second derivatives of the interfacial curve accurately in order to faithfully represent the physics. The interface velocity is given, in the case of solidification by the expression [16]

$$\rho L V_n = (k_s \nabla T_s - k_l \nabla T_l) \cdot \mathbf{N}. \tag{2}$$

Here, ρ, L, V_n and k are respectively density, latent

heat, normal velocity of the interface and thermal conductivity, N is the normal to the interface and the subscripts l,s represent liquid and solid phases. This is in fact the statement of conservation of energy for a control volume positioned at the interface. Thus, unless a field equation solver is developed to enforce this condition strictly at the interface, the interfacial velocity will be inaccurately obtained.

Keeping in view the requirements imposed on the numerical method by the physics detailed above, we design a solution methodology to track highly distorted fronts over the grid layout shown in Fig. 1(b). Two primary tasks are involved in simulating the crystal growth phenomenon, namely, interface tracking and solution of the field equations. The details are presented in Section 3. There is no ambiguity regarding the location of the interface, and the evaluation of heat fluxes through each face of the irregular polygonal control volume is performed by conventional methods [40, 41].

2. FORMULATION

The following equations are solved on the domain displayed in Fig. 2.

Heat conduction in each phase

$$\frac{\partial T_i}{\partial_t} = \alpha_i \nabla^2 T_i \quad i = l, s \tag{3}$$

and conservation across the interface, yielding an expression for the interfacial velocity, equation (2), with the boundary conditions:

$T(X, Y_l, t) = T_l$ *at the top (liquid side) and* $T(X, 0, t) = T_s$ *at the bottom (solid side), with temperature continuity,* $T_l(X_i, Y_i, t) = T_s(X_i, Y_i, t)$ *at the interface.* (4)

At the sides of the domain adiabatic conditions are imposed, i.e.

$$\frac{\partial T}{\partial N}(0, Y, t) = \frac{\partial T}{\partial N}(\Xi, Y, t) = 0 \tag{5}$$

where Ξ is the extent of the domain, along the x-direction in Fig. 2.

At the interface, the Gibbs–Thomson condition [16] is applied, in the form

$$T = T_m (1 - (\gamma\kappa/L)) \tag{6}$$

where surface tension is considered to be isotropic for simplicity.

It is important, in simulating the morphological instability phenomena, to take account of the length and time scales of the physical mechanisms. Linear stability analysis of a planar interface indicates that the critical wavelength for morphological stability is given by [13]

$$\lambda_c = O(\sqrt{(d_o l_T)}). \tag{7}$$

Here, $d_o = \gamma/L$ is the capillary length scale of the order of Ångströms, l_T is the thermal diffusion length scale, typically of O (mm). Thus, $\lambda_c = O(\mu m)$. The instability events that we are interested in all occur at the scale of λ_c. Thus, as described in ref. [26], the chosen scales are λ_c for the length scale, and $\Delta\lambda_c/l_T$ for the temperatures scale, where Δ, the applied undercooling $= T_L - T_m$, T_L being the temperature at the liquid boundary. The velocity scale is chosen to be $\mathscr{V} = O(St\alpha_L/l_T)$, where α_L is the thermal diffusivity, St is Stefan number, defined as $C_p \cdot \Delta/L$ (C_p is the specific heat), and the time scale of motion of the interface is $\tau = \lambda_c/\mathscr{V} = \lambda_c l_T/\alpha_L St$.

Non-dimensionalizing the equations above with the scales decided upon, and defining a field $\theta_i = T_i^* - T_m^*$, where T^* represents the non-dimensional temperature, we obtain the following equations for θ_i,

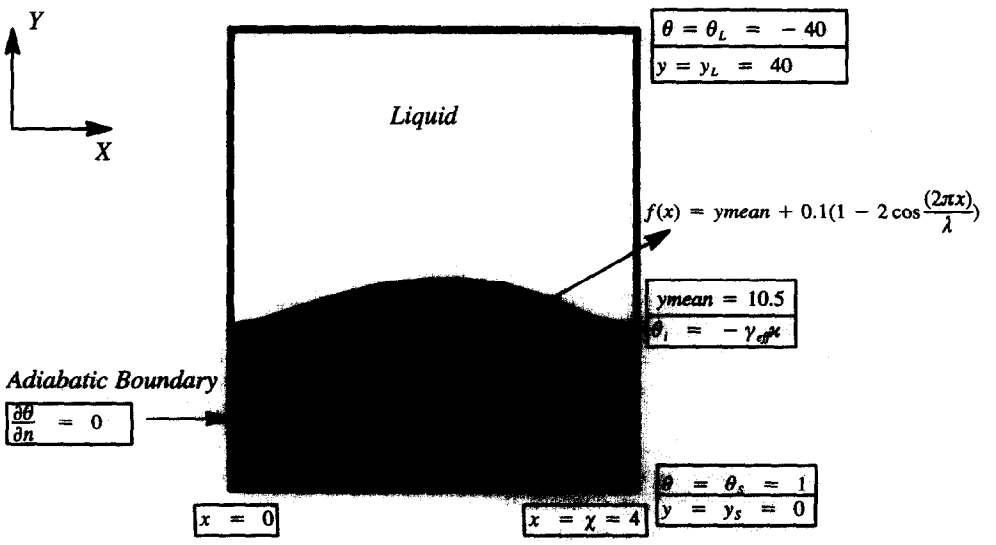

Fig. 2. Illustration of computational domain and boundary conditions in non-dimensional form.

$$\frac{\lambda_c}{l_T} St \frac{\partial \theta_i}{\partial t^*} = \nabla^{*2}\theta_i \quad i = l, s \tag{8}$$

where $\lambda_c/l_T \ll 1$ and the starred quantities are dimensionless. For the small Stefan numbers, i.e. undercoolings, usually employed in crystal growth experiments, $\varepsilon_1 = \lambda_c St/l_T \ll 1$. In our calculations we set $\varepsilon_1 = 5 \times 10^{-4}$. The interface motion equation, for the non-dimensional velocity v_n now reads

$$v_n = \left(-\frac{\partial \theta}{\partial n_L^*} + \frac{k_S}{k_L} \frac{\partial \theta}{\partial n_S^*} \right) \tag{9}$$

with the boundary conditions, $\theta(x, y_S, t) = \theta_S$ and $\theta(x, y_L, t) = \theta_L$ at the solid and liquid boundaries, (x, y) are now non-dimensional coordinates, v_n is the dimensionless velocity and $\mathbf{n}^*$ is non-dimensional normal vector.

The Gibbs–Thomson condition assumes the form, $\theta_i = -\varepsilon_2 \theta_m \gamma^* \kappa^* = -\gamma_{eff} \kappa^*$, where $\varepsilon_2 = d_o/\lambda_c$ and we designate $\gamma_{eff} = \varepsilon_2 \theta_m \gamma^*$ to be the effective surface tension. The adiabatic boundary conditions are

$$\frac{\partial \theta}{\partial n^*} = 0 \quad \text{at} \quad x = 0, \quad x = \chi \tag{10}$$

where $\chi = \Xi/\lambda_c$ is the non-dimensional domain length in the x-direction. It is noted that γ_{eff} now contains T_m and ε_2 and is dependent on both material properties and operating conditions.

Since equation (8) has the small parameter ε_1 in front of the time derivative, the temperature field is nearly quasi-stationary. Thus, the solution to the Laplace equation is imposed as the initial temperature field in each phase. The interface is perturbed in the form, $f(x, y, 0) = ymean + 0.1(1 - 2\cos(2\pi x/\chi))$. A *ymean* value of 10.5 was specified in the simulations presented here. The evolution of this initial perturbation was then followed in time.

3. THE SOLUTION METHODOLOGY

Consider the situation depicted in Fig. 1(b), which shows an interface lying arbitrarily on a grid representing part of the computational domain. The interfacial curve, as explained in [22], is tracked with the aid of marker particles indicated by crosses in the figure. Two primary tasks are to be performed in advancing the interface and thermal field in time as described below.

Given the interface position, the thermal field calculations involve the following procedures:

3.1. *To classify the control volumes and associate with them the indices of the control volume markers, if any, lying on the faces of the volumes. Only two faces of the cell are allowed to be cut by the interface as part of the marker advancing procedure*

Let us first gather all the pieces of information that knowledge of the interface location provides. Consider Fig 1(b). Joining the *interfacial markers* (Xs) with straight line segments one identifies the interfacial control volumes and obtains the *control volume markers* (filled squares), from the intersection of these segments with the grid lines. The straight line segments are consistent with the second-order accurate control volume formulation, where the field variable is assumed to vary linearly between control points. The identified interfacial cells are stored in a one-dimensional array. In each cell, the indices of the control volume (CV) markers are stored. Considering a typical control volume as in Fig. 1(b) and knowing the x and y locations of CV markers indexed n and $n+1$, other necessary details can be easily extracted to gain complete knowledge of the configuration of the control volume. In particular the intersection of the interfacial segment shown with the vertical and horizontal half cell lines are obtained. These are stored in arrays *xverthalf*(i,j),*yverthalf*(i,j), and *xhorzhalf*(i,j),*yhorzhalf*(i,j). For cells in which the horizontal or vertical half cell lines are not cut, the initial negative values assigned to these arrays are retained. Also, the midpoint of the interfacial segment is identified, and designated *xmid*(i,j),*ymid*(i,j). Thus, each interfacial cell is fully characterized in terms of the manner in which it is cut by the interface.

3.2. *To identify the phase of each computational cell*

This is easily done employing the data from Section 3.1. One traverses each column of cells starting from $j = 1$, where a flag is initialized to solid. Upon encountering a cell in which an interfacial segment lies, one determines whether the segment has crossed the vertical half-line in that cell. Three cases are likely as shown in Fig. 3(a). In case a, since *yverthalf*(i,j) lies below the control point (i,j), the flag is set to liquid in cell nj and the control point (i,j) is identified as lying in the liquid phase. In case b, since *yverthalf*(i,j) lies above the control point (i,j), the flag is set to liquid, while the control point (i,j) is identified as solid. This is done so that when the phase of cell $nj+1$ is being decided upon, the control point in that cell is identified by the flag as liquid. In case c, since the vertical half-cell line is not cut by the interface in cell nj, the flag is retained as solid, and the identification of cell $nj+1$ as a liquid cell takes place in that cell. This procedure of flag resetting is repeated upon encountering an interfacial cell once more in that column.

3.3. *Assemble the control volumes and compute the fluxes to ensure conservation*

Here, a careful rethinking of conventional differencing procedures is called for. Consider again the situation shown in Fig. 1(b). As a first step the control volume formulation is to be generalized to the polygonal (maximum five-sided) control volumes that occur at the interface. One applies Green's theorem to the typical control volume shown in Fig. 3(b). For the heat conduction equation

$$\varepsilon_1 \frac{\partial \theta}{\partial t^*} = \nabla^{*2}\theta \tag{11}$$

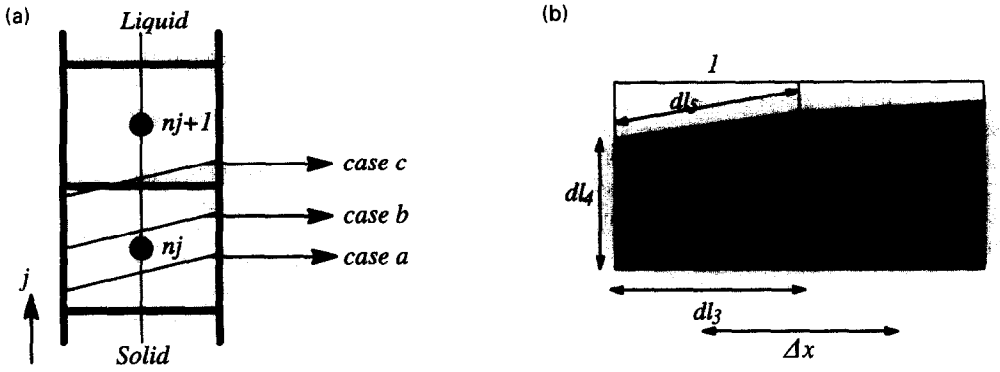

Fig. 3. Identification and nomenclature of interfacial cells. (a) Cases in the identification of phase of control volumes. (b) Nomenclature of control volume sides and dimensions.

integrating over the control volume for the 2D situation, one has

$$\int_A \varepsilon_1 \frac{\partial \theta}{\partial t^*}\, \mathrm{d}A = \int_A \nabla^{*2}\theta\, \mathrm{d}A. \tag{12}$$

Upon applying the divergence theorem, one obtains,

$$\int_A \varepsilon_1 \frac{\partial \theta}{\partial t^*}\, \mathrm{d}A = \oint_l (\nabla^*\theta \cdot \mathbf{n})\, \mathrm{d}l \tag{13}$$

where the line integral on the right represents the summation of normal fluxes out of the control volume faces. Writing the above equation in summation form,

$$\varepsilon_{1i,j}\left(\frac{\theta_{i,j}^{k+1}-\theta_{i,j}^{k}}{\Delta t}\right)A_{i,j} = \sum_{i=1}^{m}\left(\frac{\partial\theta}{\partial n}\right)_i^{k+1} \mathrm{d}l_i. \tag{14}$$

The terms $(\partial\theta/\partial n)_i$ here are the normal gradients at each control volume face, $\mathrm{d}l_i$ are the lengths of the control volume faces and m denotes the number of control volume sides (4 or 5) and $A_{i,j}$ is the area of the control volume (i,j). The superscript on the right hand side implies that an implicit scheme is to be employed. For the control volume shown in Fig. 3(b), the fluxes on faces numbered 2, 3 and 4 are easily determined. For example, for side 2 we write

$$\left(\frac{\partial\theta}{\partial n}\right)_2^{k+1} = \frac{\theta_{i+1,j}^{k+1}-\theta_{i,j}^{k+1}}{\Delta x} \tag{15}$$

where Δx is the grid spacing as shown in the figure. Thus the flux through face 2 is obtained from,

$$\left(\frac{\theta_{i+1,j}^{k+1}-\theta_{i,j}^{k+1}}{\Delta x}\right)\cdot \mathrm{d}l_2. \tag{16}$$

The length of side 2 is easily determined from the details provided by operations in 3.1. The flux through the interfacial segment, side 5, is crucial as far as interfacial behavior is concerned and will be discussed next. Before we proceed with the description of the method to evaluate $(\partial\theta/\partial n)_5$, we call attention to the interfacial normal velocity expression, equation (9). The calculation of $(\partial\theta/\partial n)_5$ serves two purposes. First, it supplies the interfacial heat flux to the temperature field calculation. Second, this quantity will be required in computing the interfacial velocity. The fact that the same procedure is used for both purposes renders the interface propagation computations consistent with the field solver.

Now consider the cell (i,j) shown in Fig 3(b). In order to obtain the normal gradient at the interfacial segment in that cell, $(\partial\theta/\partial n)_5$, we project a probe into each phase in the direction of the normal to the interface at that segment. Let the normal be given by $\mathbf{n} = n_x\mathbf{i}+n_y\mathbf{j}$. Let the length of the probe be d_p. This length is chosen so that the endpoint *xref,yref* of the probe lies in an adjacent cell. Thus an appropriate value of d_p would be the length of the diagonal of the computational cell, which will ensure this condition for all orientations of the interface. Thus, $d_p = \sqrt{(\Delta x^2+\Delta y^2)}$ is assigned. The probe then is given by, $\mathbf{d}_p = d_p(n_x\mathbf{i}+n_y\mathbf{j})$. If the value of temperature at the end point of the probe, *xref,yref* shown in Fig. 4 can be obtained, then,

$$\left(\frac{\partial\theta}{\partial n}\right)_5 = \frac{\theta(xref,yref,t)-\theta(xmid,ymid,t)}{d_p} \tag{17}$$

where $\theta(xmid,ymid,t)$ is specified, for given surface tension, from the known value of curvature at the interface there. Thus, the Gibbs–Thomson condition is incorporated in the calculation. The location $xref = xmid(i,j)+d_pn_x$ and $yref = ymid(i,j)+d_pn_y$. The cell *(iref,jref)* in which point *(xref,yref)* lies is easily identified. The phase in which *(xref,yref)* lies is known *a priori*, since, by convention the normal is specified to point from the solid to liquid. The values of normal gradients in each phase are therefore extracted by projecting probes into both phases along the same direction.

Now, to obtain the value of temperature $\theta(xref,yref,t)$, a biquadratic shape function is fit to the temperature field in the vicinity of the interface. The six coefficients appearing in the biquadratic form, $F(x,y) = ax^2+bxy+cy^2+dx+ey+f$, are obtained by choosing six cells in the *same phase* around the point *(xref,yref)* and inverting the resulting 6×6 matrix by a Gaussian elimination procedure. In this process, it is also to be ensured that the six points

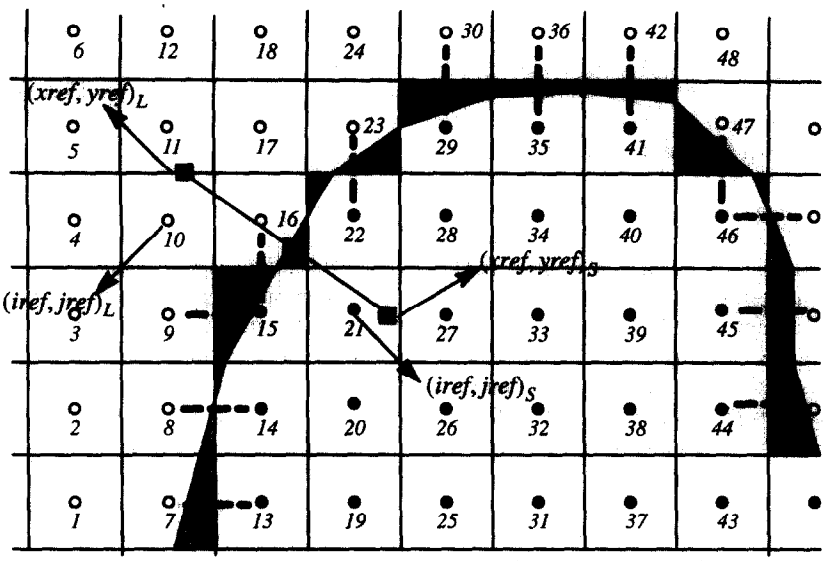

Fig. 4. Illustration of cut cells, partner cells and method for determining the normal gradient at the interface (see cell 16). Normal is projected from point (xmid,ymid) in cell 16 along the normal at that point. The probe of length d_p ends at the points (*xref,yref*) in each phase. (*iref,jref*) is the index of cell in which (*xref,yref*) lies. Solid phase control points are denoted by filled circles, liquid by open circles Partner cells are indicated by the linkages between cells.

chosen for fitting the biquadratic should cover three i and three j levels, which is obviously necessary for a biquadratic representation to be valid. For example, in the case of the cell 16, the probe, extended from the point (*xmid,ymid*) in that cell, ends in cell 10. In order to obtain the value of temperature at the point (*xref,yref*) which lies in the liquid phase, we need to choose six cells in the liquid phase. The choice of five cells is straightforward in this case. These are cells numbered 4, 16, 11, 9 and 10 itself. The sixth cell remains to be chosen. Depending on which quadrant of the cell 10 the point (*xref,yref*) lies, the cell along the diagonal that is closest is picked. In this particular example, that cell is numbered 17. Similarly for the temperature at $(xref,yref)_S$, i.e. in the solid phase, cells 15, 21, 27, 22, 20 and 26 are used. Thus, once $\theta(xref,yref,t)$ is obtained from the functional form, the normal flux is obtained in each phase from equation (17). The $\partial\theta/\partial n$ value in the *same phase* as the control point (i,j) is then fed into the control volume expression for that cell. Thus, the flux through each face of the control volume shown in Fig. 3(b) has now been obtained.

To ensure conservation in the vicinity of the interface, however, several other procedures are necessary. Consider cells numbered 29 and 30 in Fig. 4. Between the two control volumes, there is a trapezoidal piece, shown hatched, that is unaccounted for. To enforce conservation, it is necessary that the flux across the interface computed for cell 29 as described above be transmitted to cell 30. This procedure involves the identification of three types of cells:

(a) *Bulk cells.* A cell that has all its neighbors in the same phase. The control volume formulation for such cells is straightforward.

(b) *Interface adjoining cell.* A cell, such as cell 30, that has a neighbor in the opposite phase, but is not itself an interfacial cell.

(c) *An interfacial cell.* A cell, such as 29, through which the interface passes.

To enforce conservation, for cells of type (b) and (c) we need to identify *partner cells.* The choice of partner cells has been indicated in Fig. 4 for each cell by the linkages shown. Each interfacial cell is assigned one or more partner cells (for example cells numbered 9, 15, 16). When the control volume fluxes are assembled for the interfacial cells, the fluxes into the designated partner cells are modified appropriately. For example, let cell 29 belong to the solid phase, and cell 30 lie in the liquid. While performing the flux calculations for cell 29, we compute the $\partial\theta/\partial n$ value in each phase at the interface. The flux $\partial\theta/\partial n$ value in the liquid phase is then transmitted to cell 30. We recall that these fluxes also go into determining the normal velocity of the interface thereby maintaining consistency. In addition, the control volume shape and area of the partner cell are redefined, so that the cell 30, for instance, absorbs the hatched trapezoidal region. In other words, partner cells need to be identified and handled unless the interface happens to coincide with a grid line, which is generally not the case. Thus there are no missing pieces in the mosaic of control volumes and all the hatched regions are incorporated into the appropriate partner cells, along with the fluxes at the interface. This assembly process is not difficult to execute. The procedures only apply to the one-dimensional interfacial cell array. The eight separate cases of interfacial cell and partner types are shown in Fig. 4. The control volume flux assembly procedures have been checked for symmetry by exam-

ining the numerical values of the difference coefficients for a specified symmetric interface shape and letting it evolve over time. Also, the cell assembly direction was reversed, so that the interfacial cell and its partner exchanged roles, which yielded identical results.

3.4. *Compute the temperature field*

Once the fluxes have been assembled for all the cells in the domain, the solution for the temperature field is performed with an iterative procedure, fully coupled with the interface motion. The alternate line SOR procedure is employed, leading to a tridiagonal matrix equation which is easily solved. The feature of importance is that, over each iteration, the interface is updated, along with the temperature field in each phase, and the converged solution yields the thermal field as well as interface position at the new time level. At this stage, we have already obtained the information necessary for computing the normal velocities of the interface. However, the gradients $(\partial\theta/\partial n)_{l,s}$ are now available at the locations (*xmid,ymid*) in each control volume. However, the interfacial markers are not usually located at the points (*xmid,ymid*). Thus, one has to obtain the value of the temperature gradients at the locations of these markers, in order to calculate their velocities. To transmit this information to the locations of the interfacial markers, we utilize the array corresponding to the locations (*xmid,ymid*) along the interface. The value of the arclength at each point (*xmid,ymid*) while traversing the interface is obtained and the $(\partial\theta/\partial n)_{l,s}$ values fit to piecewise quadratic functions of arclength, i.e.

$$\left(\frac{\partial\theta}{\partial n}\right)_{l,s} = a_i\psi^2 + b_i\psi + c_i \tag{18}$$

where ψ is the arclength along the interface in the ith interface segment and a, b and c are coefficients to be determined. Thus, knowing the value of ψ corresponding to the interfacial marker locations one can identify the segment in which the point lies and thus the value of $(\partial\theta/\partial n)_{l,s}$ can be calculated from the appropriate functional form. The interfacial marker is then translated along the normal **n**.

4. RESULTS AND dISCUSSION

4.1. *Grid addition and deletion*

The computational domain is configured as shown in Fig. 5. The domain is partitioned into three regions. Coarse grids are employed in the regions I and III, away from the interface, while fine grids are employed in the region II close to the interface. However, as the interface rapidly grows out of region II there is a need for introducing a fine grid that precedes the interface in order to be able to calculate the gradients ahead of it with desired accuracy. To achieve this, grid lines are added such that a sufficiently extended region ahead of the interface is replenished with fine grids, throughout the evolution of the interface. The values of field variables in this region are obtained by linear interpolation. The grid addition takes place at a frequency depending on the extent of the domain traversed by the interface.

4.2. *Planar interface propagation*

We first test the solution scheme for accuracy by employing known exact solutions for a planar interface. The Neumann solution for an interface that is melting is given by [45]

$$\theta(x,y,t) = 1 - \mathrm{erf}\left(\frac{y-y_l}{2\sqrt{t}}\right)\Big/\mathrm{erf}(\xi) \tag{19}$$

$$S(t) = y_l - 2\xi\sqrt{t} \tag{20}$$

where $\theta(x,y,t)$ is the temperature, $S(t)$ is the interfacial position, and ξ is given by the relation

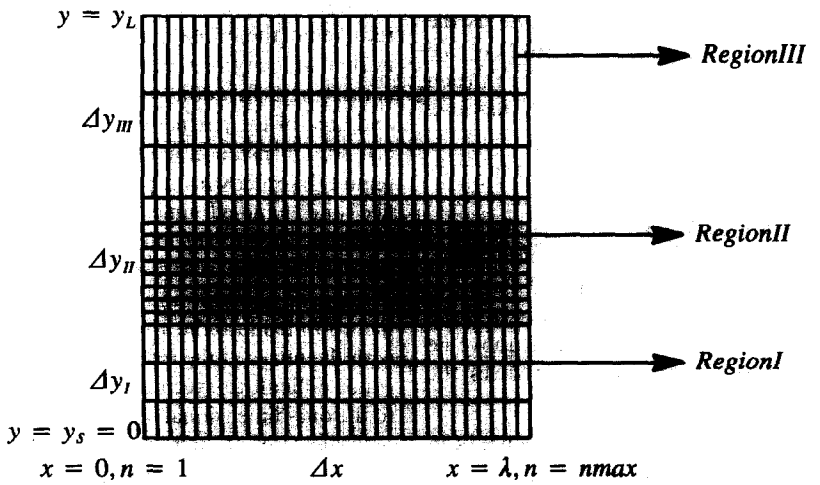

Fig. 5. Grid arrangement for the computational domain. Region II extends along with the interface.

$$\xi e^{\xi^2} \operatorname{erf}(\xi) = \frac{St}{\sqrt{\pi}} \tag{21}$$

St is the Stefan number given by $C_p (T_I - T_m)/L$. The boundary conditions are, $\theta(x, y_l, t) = 1$, i.e. at the top of the boundary, y_L is fixed and $\theta(x, y, t) = 0$, $Y \leqslant S(t)$, i.e. the solid is at uniform temperature. The initial conditions are specified at time $t_o > 0$, taking account of the singularity at $t = 0$. Thus,

$$\theta(x, y, t_o) = 1 - \operatorname{erf}\left(\frac{y - y_l}{2\sqrt{t_o}}\right) \Big/ \operatorname{erf}(\xi) \tag{22}$$

and the initial interface location is given by the expression,

$$S(t_o) = 2\lambda\sqrt{(t_o)} \tag{23}$$

where λ is a constant. Figure 6 (upper) compares the exact and numerical solutions obtained for Stefan number $St = 0.1303$, $\xi = 0.25$, $y_l = 4$. A 41×41 grid is used. The initial position of the interface was at $y = 3.91$. The computation was performed for 1000 time steps and over the period of calculation the computed and exact interface locations as well as temperature fields are in excellent agreement.

A more stringent test of the planar interface propagation is in computing the higher Stefan number case, $St = 2.8576$, $\xi = 0.9$, shown in Fig. 6 (lower). The computations are performed with 61 grid points along the y-direction. Again excellent agreement is obtained for computations over 100 time steps. For this higher Stefan number case, the interface moves more rapidly and a significant portion of the domain ($Y_l = 4$) has

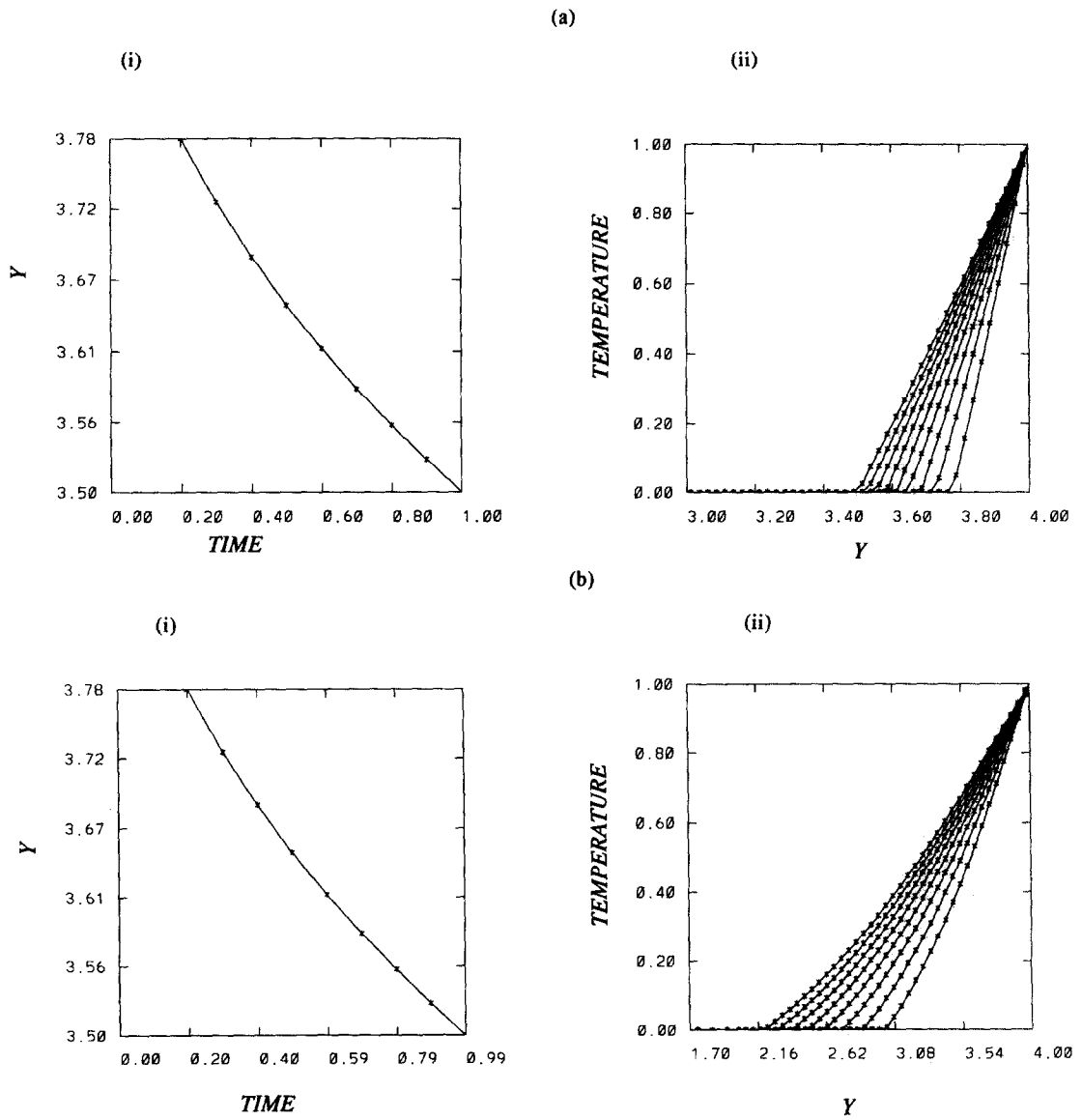

Fig. 6. Comparison of exact (* symbol) and computed (line) solutions for different Stefan numbers for propagation of a planar interface. (i) For Stefan number = 0.1303: (a) interface position against time; (b) temperature along Y at different times. (ii) For Stefan number = 2.85, (a) interface position against time; (b) temperature along Y at different times.

been traversed by the interface. From the above examples, it is clear that for a planar interface, the conservation statement across the interface is honored by the control volume formulation and the interface position is accurately obtained for a wide range of Stefan numbers.

4.3. *Non-planar interfaces*

In the computations to follow, we employ *nmax* grid points along the x-direction, where *nmax* was 21, 41 or 81. Since $\chi = 4$, and $y_1 = 40$ in all subsequent calculations, we have $\Delta x = 4/nmax$. Depending on the value of Δx, we employ grid points in the region II, such that $\Delta y_{II} = \Delta x$. As mentioned before, as the interface grows and propagates grids are added ahead of and deleted behind the interface. Thus the extent of region II increases as the computation proceeds. The domain of computation is shown in Fig. 2. The liquid end was maintained at $\theta_1 = -40$, with the solid side at $\theta = 1$. The side boundaries are adiabatic, i.e. $\partial\theta/\partial x = 0$. The Stefan number for the system is 1 as obtained from the scaling procedure. Thus, the solidification process is being viewed not at the diffusion time scale, but at the time scale corresponding to interface motion. With this scaling, the heat conduction equation is nearly quasistationary.

4.3.1. *Zero surface tension.* The evolution of an isothermal interface was tracked on grids with *nmax* = 21, 41 and 81. The results are presented in Fig. 7. Clearly, for the isothermal interface the results are governed to a large degree by the grid spacing. The behavior of interfaces with zero surface tension has been under scrutiny, with calculations indicating cusp-formation or tip-splitting [46]. Since, *in the absence of surface tension, no stabilization mechanism exists at any length scale*, i.e. there is no smoothing effect, *disturbances of all wavelengths are amplified.* Thus, finite-time singularities can form on the interface. Our calculations show that on the *nmax* = 21 grid, displayed in Fig. 7(a), *the perturbation grows for the period of calculation and loses symmetry*. The source of asymmetry comes from the uni-directional procedure used to define the interface shape and temperature gradients. For *nmax* = 41, Fig. 7(b), the interface first loses its symmetry, similar to the 21 grid case, and as time elapses, the perturbation wavelengths permitted by the grid lead to a *tip-splitting instability*. A trough is formed upon tip-splitting, and rapid accumulation of latent heat ensues there, leading quickly to the formation of a cusp in that region. Thus, the sharp corner created there cannot be smoothed out in the absence of surface tension. For an even finer grid, *nmax* = 81, as shown in Fig. 7(c) the interface becomes unstable to grid-scale oscillations. These *short wavelength oscillations grow faster than the disturbances that are captured on the coarser grid and a cusp rapidly forms at the boundary where the imposed periodicity condition becomes incompatible with the asymmetric breakdown of the interface.* The results on this fine grid correspond to our previous results obtained by employing boundary-fitted adaptive grids [26]. There, in the absence of surface tension, the cusp formed at the boundary, and short wavelength oscillations developed on the interface. The simulation in this case could, however, be carried farther than previously, because the grid is not required to conform to the interface. The behavior of the interface under different grid resolutions has been investigated. *It is interesting that with the different grid resolutions, different modes of instability, including asymmetry, singularities and tip-splitting can appear.* Figure 7 indicates that there is no preferred morphological shape for the zero surface tension case. Furthermore, because there is no prevailing physical length scale contained by the instability development itself, the numerical resolution, in effect, controls the smallest length scales of the instability. As the grid is refined, finer instability scales appear, implying that no grid independent solution can be obtained with zero surface tension. It is noticed in each case that asymmetry develops in the interface profiles. It was found in most of our calculations where the interface was highly unstable (i.e. for zero and low surface tensions) that asymmetric breakdown persisted. In addition, the breakdown always occurred on the same side of the domain, namely on the left. Such asymmetric breakdowns have been remarked upon in connection with experiments on the Saffman–Taylor instability [5] and in the boundary integral simulations of ref. [30]. In the latter, when symmetry was not imposed, the interface became unstable asymmetrically. When sufficient surface tension is present, it will be shown that the asymmetry is eliminated. Thus, for the highly sensitive low surface tension cases, any small noise generated in the course of the computation leads to a breakdown of the smooth perturbation. Here the first appearance of asymmetry comes from the bias of the line iterative procedure in the course of computation. The other procedures, namely assembly of control volumes, definition of partner cells and interface definition were performed in the reverse order and the asymmetry was found to persist.

4.3.2. *Low surface tension.* The sensitivity of the solution procedure can be demonstrated by adding a surface tension $\gamma_{\text{eff}} = 10^{-3}$ where, as defined previously, $\gamma_{\text{eff}} = \varepsilon_2\theta_m\gamma^*$. Since the curvature is O(1), the Gibbs–Thomson condition [16] will lead to interface temperature variations of $O(10^{-3})$. This modification of the temperature at the interface is extremely small when compared to the non-dimensionalized undercooling value $T_1 = -40$ imposed at the liquid boundary. When this small value of surface tension is added for the *nmax* = 81 calculation, it eliminates the singularities at the interface. However, the perturbations along the interface continue to grow. Following the interface evolution further, a series of instabilities develop in the vicinity of the tip and result in the asymmetric convoluted structure shown in Fig. 8(a). The interface is highly distorted in this case, demonstrating the ability of the numerical technique

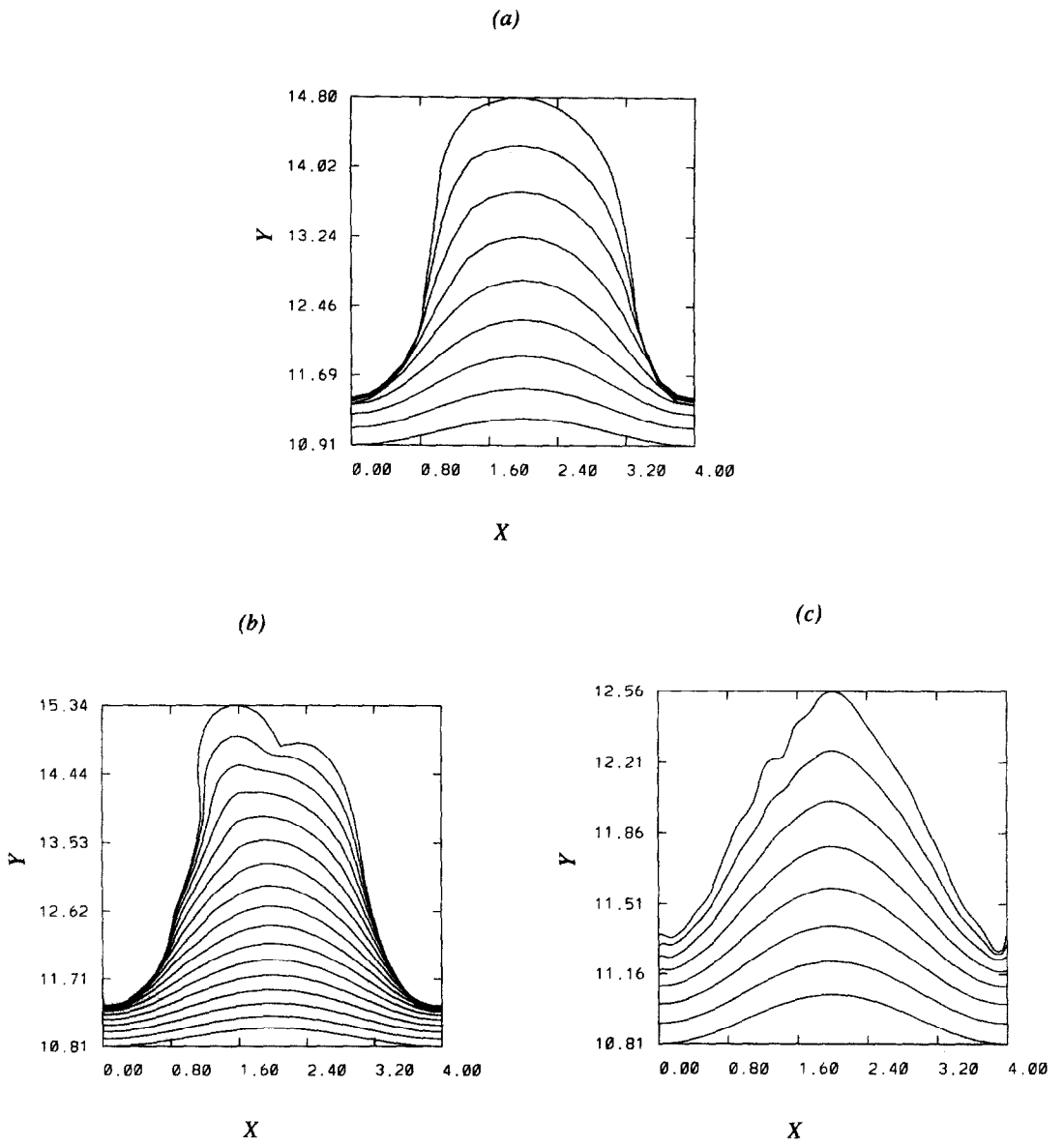

Fig. 7. Development of interface for zero surface tension for various grid resolutions. (a) Interface shapes at different time instants for $nmax = 21$ grid, up to time = 1.8, in steps of $dt = 0.2$. Symmetry is broken in this case. (b) Interface shapes for $nmax = 41$ grid, up to time = 1.8, in steps of $dt = 0.1$. In this case symmetry is first broken, and tip-splitting follows. (c) Interface shapes for $nmax = 81$ grid, up to time = 0.8 in steps of $dt = 0.1$. Computations were stopped early in this case due to cusp formation at the boundary. Note that shorter wavelengths are allowed on this finer grid, which become unstable more rapidly.

developed here to handle such strongly multiple-valued shapes. It is also noted that, while one side of the interface appears to break into a cascade of protuberances in the vicinity of the tip, the other side remains quite stable. The further development of the side branches is found to be arrested due to the accumulation of heat in the sides of the growing finger. The imposition of the adiabatic side-wall condition prevents the removal of heat from this region. Figures 8(b) and (c) show the isothermal contours in the vicinity of the interface in the early and later stages of the development shown in Fig. 8(a). As is clearly seen, the temperature field calculation responds to the highly distorted nature of the interface, even for such a low value of the interface temperature. Furthermore, the clustering of the isotherms to the left of the tip clearly drives the instability in that region, leading to a mutually enhancing dynamic process between the interface and thermal field. In comparison the isotherms on the right side are seen to be less crowded. With regard to the question of asymmetry, as already pointed out, this feature results from the fact that our cell cutting procedure is conducted along a given direction, which can create initial noises along that direction. These initial noises, once formed, influence the paths of subsequent development morphologically. However, this

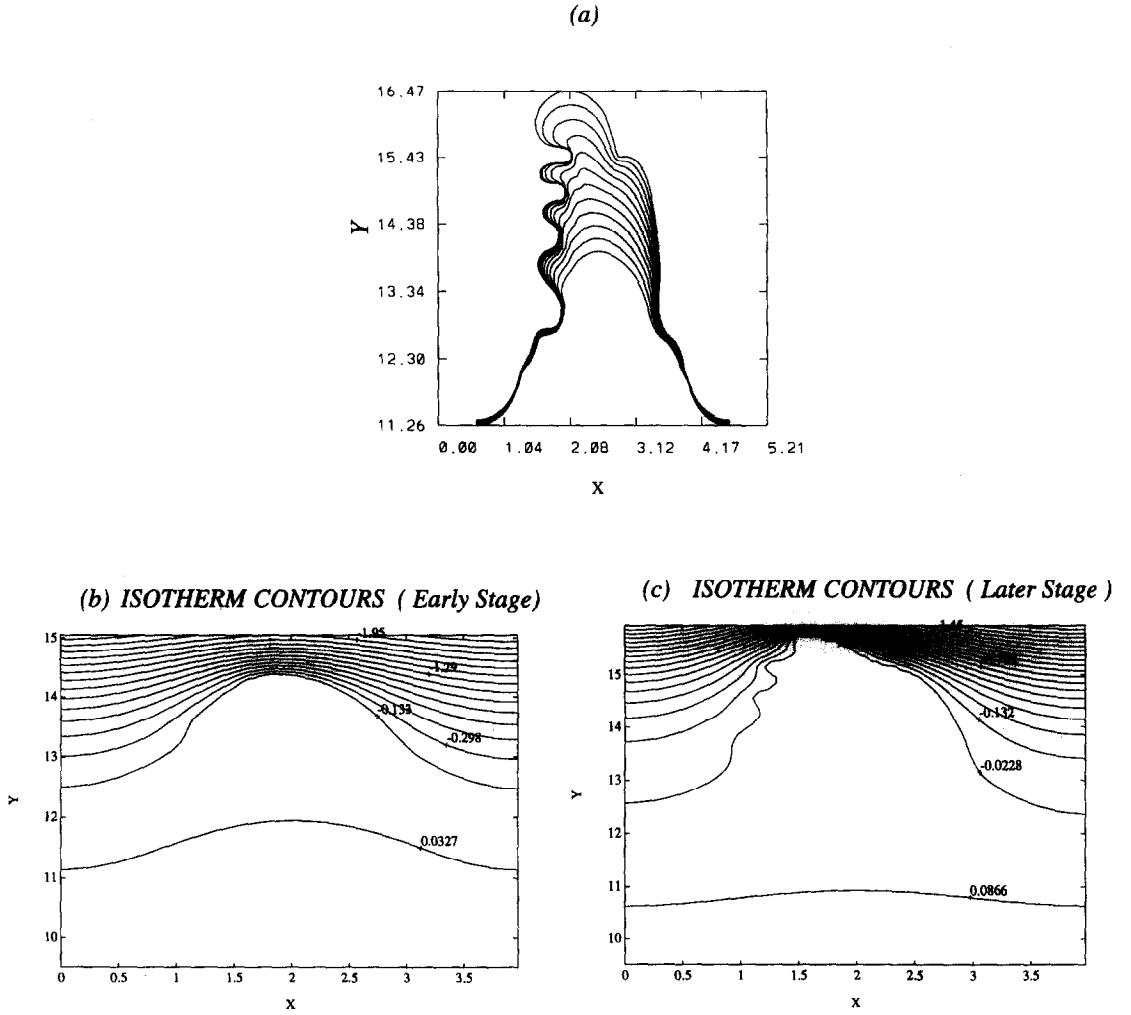

Fig. 8. Development of interface for low surface tensions (10^{-3}) on $nmax = 81$ grid. From time $t = 0.8$ to $t = 2.0$. (a) Interface shapes at different time instants showing successive instabilities. (b) Isotherm plot at early stage showing asymmetry. (c) Isotherms at later stage showing response of thermal field to distorted interface even for the very low value of surface tension.

aspect does not affect the solution accuracy when surface tension plays a more substantial role, as will be discussed later.

For low surface tension cases computational studies that impose symmetry result in interface patterns different from those without such constraint, due to the fact that the morphology of the interface is highly path dependent. Any change in the boundary conditions or computational details will create different numerical noises, which in turn, yield different final interface shapes. To illustrate the impact of enforcing symmetry on the interface for low surface tension, we compute the development of only half the perturbation by imposing symmetry condition for the other half. For the $nmax = 81$ case, with low surface tension $\gamma_{eff} = 10^{-3}$, the resulting symmetric structure is shown in Fig. 9(a). There is again a series of instabilities in the vicinity of the tip reminiscent of the structures observed in the Saffman–Taylor experiments with tip bubbles [47]. On a finer grid, $nmax = 161$, a similar phenomenon results, as shown in Fig. 9(b), except that in this case the tip breaks down at shorter wavelengths, and the instability development is much more rapid than in the case of the coarser grid calculations. Thus, imposition of symmetry does not influence the stability of this low surface tension interface. The shape of the computed interface is however, very different from the case where symmetry is not explicitly imposed i.e. Fig. 8(a). Nevertheless, the changing wavelengths in both Figs. 8 and 9 indicate that grid resolution is the main cut-off length scale with zero or low surface tension. It should be clarified however that, as long as surface tension is non-zero, there exists a physical length scale to control the morphological length scale of the interface. The results discussed so far, however, are for very low surface tensions, which creates a length scale too small to be resolved by the grid spacing employed here. With zero surface tension, existing theory indicates that no grid independent solutions exists [16];

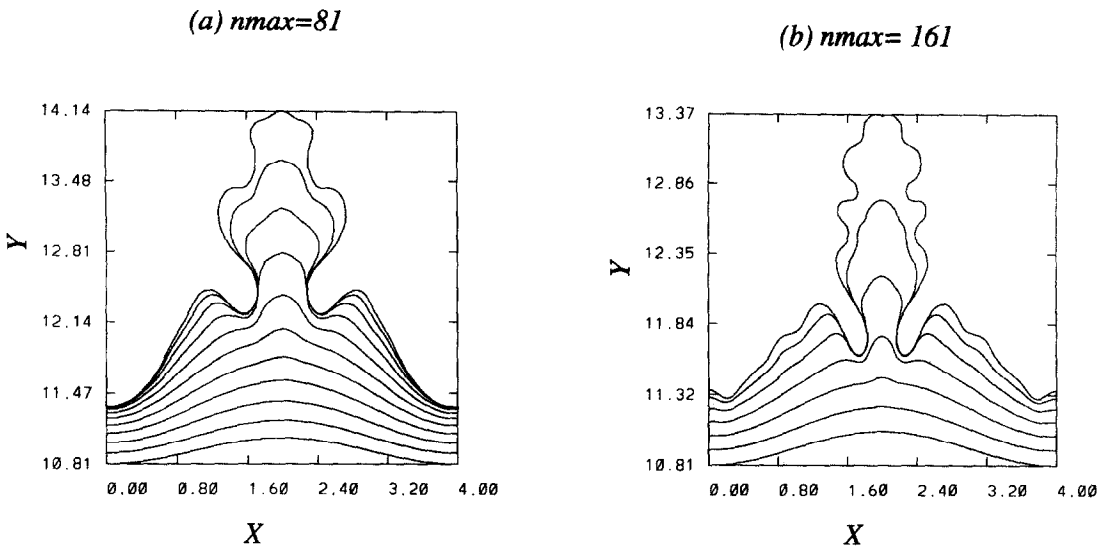

Fig. 9. Effect of imposition of symmetry on development of interface for low surface tension ($\gamma_{eff} = 10^{-3}$): (a) on $nmax = 81$ grid (b) on $nmax = 161$ grid. Interface shapes are shown after reflection across the centerline.

with a finite surface tension, however small it is, unique solutions do exist, and the issue then is numerical resolution. To ascertain the numerical accuracy of the present algorithm, a higher effective surface tension is considered next.

4.3.3. *Stable fingers for higher surface tensions.* The extreme sensitivity of the low surface tension cases to grid spacing, which yields widely different behaviors upon refinement, prompts us to confirm grid independence for the more stable higher surface tension cases. As already explained, this exercise can be conducted only for non-negligible effective surface tension cases. It should be again emphasized that the so-called low and high surface tensions are defined with respect to our grid resolution. Furthermore, it is the effective surface tension under consideration here, which involves both material properties and operating conditions, and hence can vary substantially. Figure 10(a) compares the interface shape and velocity of an interface with $\gamma_{eff} = 10^{-2}$, $nmax = 41$ (full lines) and $nmax = 81$ (open circles). While in the initial stages of development the profiles as well as interface velocities are in agreement, as the perturbation develops to large amplitudes the coarser grid calculation underestimates the instability magnitude. In fact the final stage of the fine grid calculation shows a vastly different value of velocity. Figure 10(b) compares the same interfacial development for $nmax = 81$ (full line) and $nmax = 161$ (open circles). As can be seen, the two calculations maintain close consistency, even in the large amplitude stage. The velocities in the final stage are in close agreement. Thus, for high enough surface tension, grid effects are suppressed and the stable finger growth converges under grid refinement. In subsequent calculations we employ $nmax = 81$.

Next, we present results of long time simulation of two different γ_{eff} to further contrast the effect of surface tension. Figure 11 shows the development of a finger for $\gamma_{eff} = 10^{-2}$, along with the derivatives along the interface. The first observation to make regarding these results is the well maintained symmetry of the front. Figure 12 shows the development of the finger for $\gamma_{eff} = 10^{-1}$. The interfaces are shown at the same instants of time. The effects of surface tension are brought forth by comparing these two sets of results. The qualitative features are in agreement with the computations of ref. [31], who used the boundary element method. In particular, the rapid accumulation of heat on the sides of the finger leads to a rapid slowdown of the interface in that region. The front propagates upward farther in the higher surface tension case before the instability gathers momentum. The amplitude of the $\gamma_{eff} = 10^{-2}$ finger (aspect ratio ≈ 4) is greater than the $\gamma_{eff} = 0.1$ finger (aspect ratio ≈ 2.5), demonstrating the higher degree of instability for lower surface tension. The higher surface tension (10^{-1}) causes the finger to spread laterally, leading to a multiple-valued interface with respect to x. The sides of the lower surface tension (10^{-2}) finger are almost flat and vertical, indicating minimal lateral spreading. The circular arc fits for representing the interfacial segments hold up very well even for such a flat vertical surface. The finger in the higher surface tension case has a more rounded tip and there is a wide region near the tip where the curvature is nearly constant. In contrast, the $\gamma_{eff} = 10^{-2}$ finger is sharper at the tip. At the stage of the development shown, as seen from the plots of interfacial derivatives against x, the interfaces in both cases appear to have attained stable, shape-preserving growth. However, as observed by Saffman and Taylor [3], over a substantial length and time, the growth velocity of the finger is not constant and the tip is still accelerating, due to the finite domain size in our calculation. As the finger

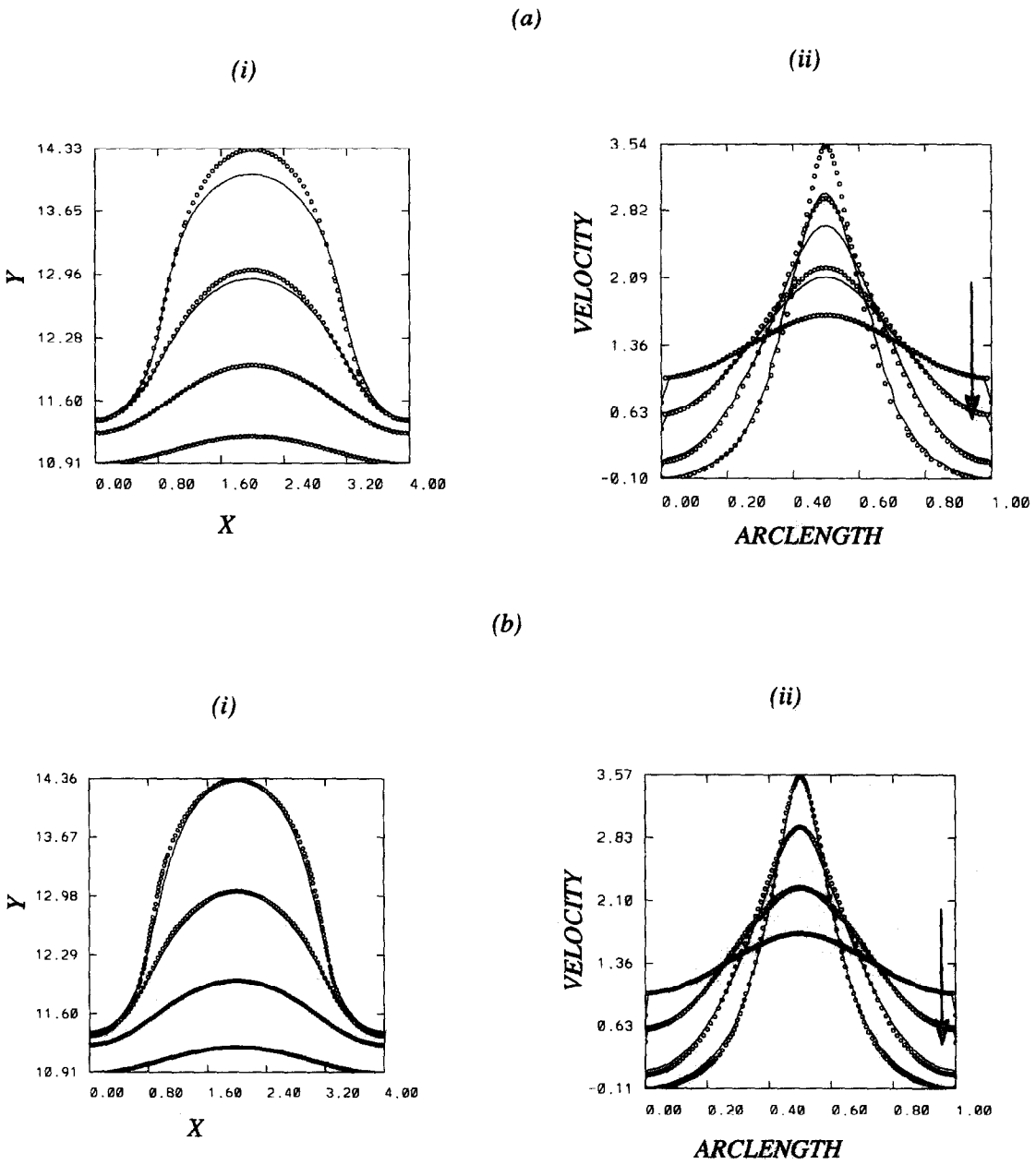

Fig. 10. Comparison of solutions for surface tension $\gamma_{\text{eff}} = 0.01$ on $nmax = 81$ (full lines) and $nmax = 161$ (open circles). (a) $nmax = 41$ (full lines) and $nmax = 81$ (open circles) grids. (b) $nmax = 81$ (full lines) and $nmax = 161$ (open circles) grids. (i) Interface shapes at different time instants. (ii) Interface velocities at time instants corresponding to (i).

reaches an asymptotically invariant shape, the tip velocity will approach a constant value.

Figure 12(b) shows the isotherms in the vicinity of the interface for the $\gamma_{\text{eff}} = 0.1$ case. The finger in this case extends from about $Y = 12$ to 21. Clearly the clustering of the isotherms at the tip drives the instability. The Gibbs–Thomson effect causes the isotherm corresponding to $\theta = -2.2 \times 10^{-2}$ to curve inward in the tip region where the curvature is positive. The symmetry of the isotherms confirms our previous statement regarding the ability of the surface tension to suppress asymmetry. Figure 12(c) shows isotherms across the interface. The effect of the Gibbs–Thomson condition is seen to propagate far down the solid finger, as evident from the curvature of the -2.19×10^{-2} isotherm at Y = 18, which is well into the solid finger. The curvatures of the isotherms however change sign further down, as for the $\theta = 3.53 \times 10^{-3}$ isotherm. The isotherm plot for $\gamma_{\text{eff}} = 0.01$, Fig. 11(b), shows no sign of the Gibbs–Thomson condition for the available contour resolution. The first negative isotherm is in the correct position since the tip of the finger is located

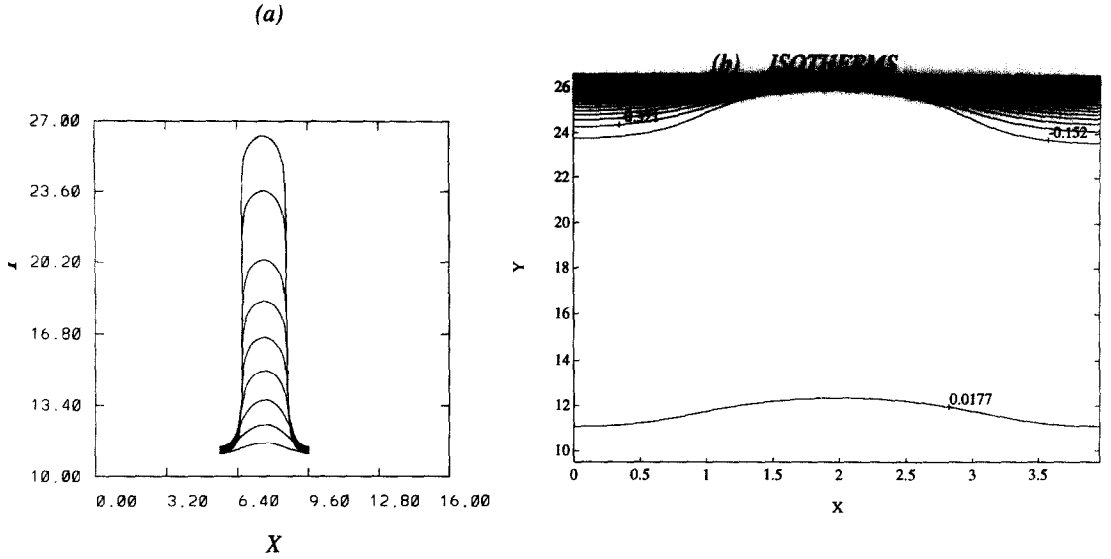

Fig. 11. Development of solutions for surface tension $\gamma_{\text{eff}} = 0.01$. Up to $t = 4.0$. (a) Interface shapes at equal intervals of time. The finger has been drawn to scale. (b) Isotherm contours including entire interface.

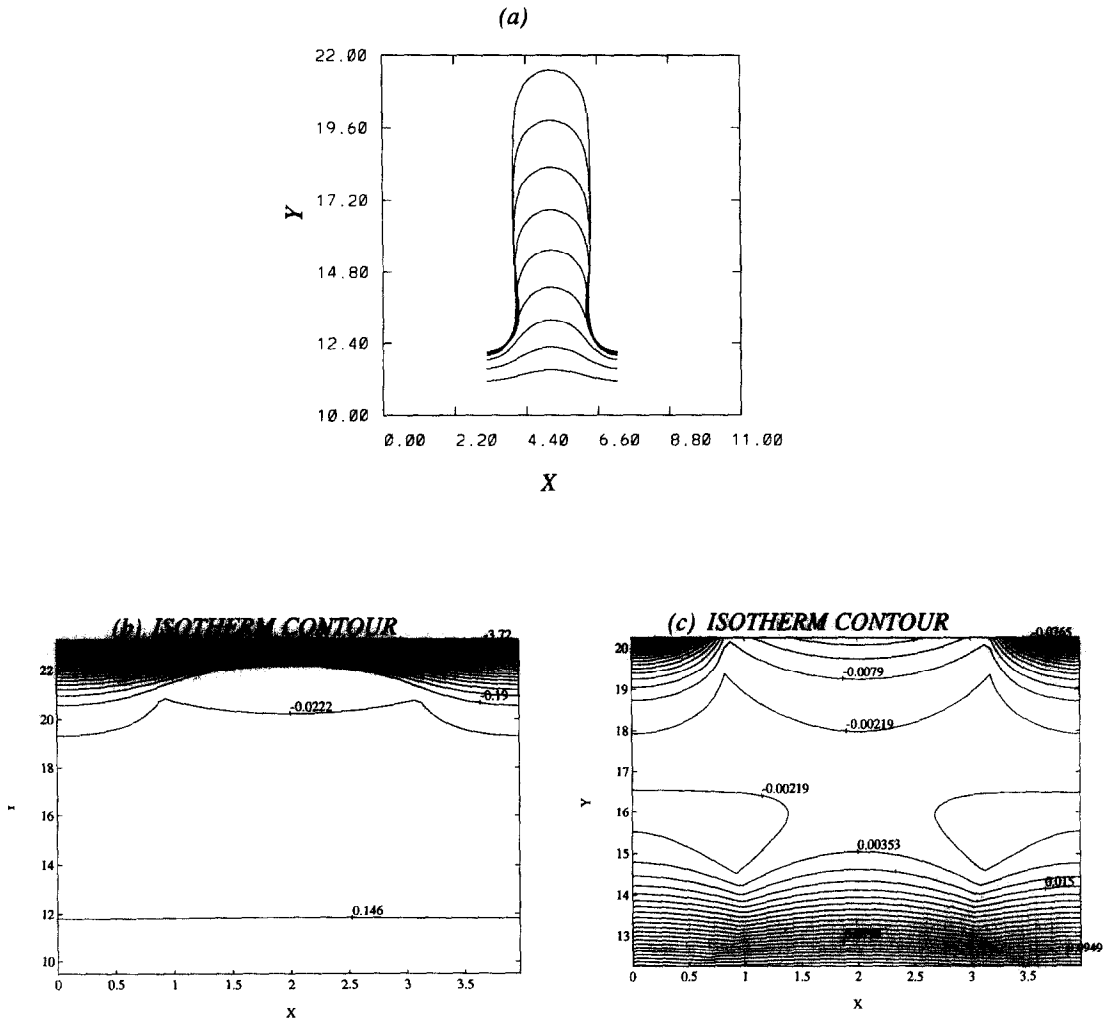

Fig. 12. Development of interface for surface tension $\gamma_{\text{eff}} = 0.1$. Up to $t = 4.0$. (a) Interface shapes at equal intervals of time. The finger has been drawn to scale. (b) Isotherm contour for entire finger. (c) Isotherm contour for portion of finger not including tip.

approximately at $Y = 27$, in agreement with the isotherm plot.

5. CONCLUSIONS

We have presented a method for tracking highly distorted fronts on fixed Cartesian grids. The facility afforded by the Cartesian grid, in terms of setting up the control volume formulation, leads to a capability of handling the morphologically complex moving interface. In contrast with other Eulerian methods, it is possible here to explicitly specify the location and shape of the interface and to apply the boundary conditions at the exact location of the interface. In strictly Lagrangian methods, on the other hand, the grid translates with the interface and needs to be periodically smoothed and redistributed. The non-boundary-fitted grid layout here circumvents such problems.

For a planar interface the Neumann solutions for a melting problem have been accurately reproduced by the numerical solutions. In a follow-up work, detailed comparison has been made between the present algorithm and a body-fitted computational method in the context of irregularly-shaped phase boundary [48]. Favorable agreements have been obtained for several different test problems, with and without a moving boundary. The results for the deformed interface illustrate the effects of surface tension. In the absence of surface tension, singularities quickly develop on the front for sufficient grid resolution. The grid resolution governs the wavelength of noise permitted on the interface and thus affects interfacial development. In particular, at very low surface tensions the disturbances allowed by the grid strongly influence the fate of the interface. These aspects are all consistent with the existing theory [1, 12, 16]. Thus care needs to be exercised in interpreting results in this range of surface tension parameter. For sufficient interfacial tension, the results have been demonstrated to converge under grid refinement. The initial perturbation develops in time into long fingers, as in the Saffman–Taylor problem. The qualitative features are in agreement with other simulations of the fingering phenomenon. The finger shapes reached a steady-state, while the tip accelerated due to the fixed domain size and boundary conditions.

REFERENCES

1. D. A. Kessler, J. Koplik and H. Levine, Pattern selection in fingered growth phenomena, *Adv. Phys.* **37**(3), 255–339 (1988).
2. U. Nakaya, *Snow Crystals*. Harvard University Press, Cambridge, MA (1954).
3. P. G. Saffman and G. I. Taylor, The penetration of a fluid into a porous medium or Hele–Shaw cell containing a more viscous fluid, *Proc. R. Soc. Lond. A* **245**, 312–329 (1958).
4. D. Bensimon, Stability of viscous fingering, *Phys. Rev. A* **33**, 1302–1308 (1986).
5. P. Tabeling, G. Zocchi and A. Libchaber, An experimental study of the Saffman–Taylor instability, *J. Fluid Mech.* **177**, 67–82 (1987).
6. M. C. Flemings, *Solidification Processing*. McGraw-Hill, New York (1974).
7. D. P. Woodruff, *The Solid–Liquid Interface*. Cambridge Press, Cambridge, U.K. (1973).
8. J.-M. Flesselles, A. J. Simon and A. J. Libchaber, Dynamics of one-dimensional interfaces: an experimentalist's view, *Adv. Phys.* **40**(1), 1–51 (1991).
9. P. Huerre, Spatio-temporal instabilities in closed and open shear flows. In *Instabilities and Nonequilibrium Structures* (Edited by E. Tirapegui and D. Villaroel), pp. 141–177. Reidel, Dordrecht (1987).
10. D. H. Sharp, An overview of Rayleigh–Taylor instability, *Physica* **12D**, 3–18 (1984).
11. P. G. Drazin and H. W. Reid, *Hydrodynamic Stability*. Cambridge University Press, Cambridge (1981).
12. J. S. Langer, Instabilities and pattern formation in crystal growth, *Rev. Mod. Phys.* **52**(1), 1–56 (1980).
13. J. S. Langer and Muller-Krumbhaar, Theory of dendritic growth—I, II and III, *Acta Metall.* **28**, 1681–1708 (1978).
14. M. E. Glicksmann and S.-C. Huang, Fundamentals of dendritic solidification—I and II, *Acta Metall.* **29**, 701–734 (1981).
15. P. Pelce, *Dynamics of Curved Fronts*. Academic Press, New York (1988).
16. W. Shyy, *Computational Modelling for Fluid Flow and Interfacial Transport*. Elsevier, Amsterdam, The Netherlands (1994).
17. R. Pieters and J. S. Langer, Noise-driven sidebranching in dendritic crystal growth, *Phys. Rev. Lett.* **56**, 1948–1952 (1986).
18. M. Rappaz, Modelling of microstructure formation in solidification processes, *Int. Mater. Rev.* **34**(3), 93–123 (1989).
19. R. A. Brown, Theory of transport processes in single crystal growth from the melt, *A.I.Ch.E. J* **34**, 881–911 (1988).
20. S. Ostrach, Fluid mechanics in crystal growth, *J. Fluids Engng* **105**, 5–20 (1983).
21. Ph. Bouissou, B. Perrin and P. Tabeling, Influence of an external periodic flow on dendritic crystal growth. In *Nonlinear Evolution of Spatio-temporal Structures in Dissipative Dynamical Systems* (Edited by F. H. Busse and L. Kramer). Plenum Press, New York (1990).
22. H. S. Udaykumar and W. Shyy, Development of a grid-supported marker particle scheme for interface tracking, *11th AIAA Comp. Fluid. Dyn. Conf.*, Paper No. AIAA-93-3384, Orlando, Florida (1993).
23. J. Glimm, J. Grove, B. Lindquist, O. A. McBryan and G. Tryggvason, The bifurcation of tracked scalar waves, *SIAM J. Sci. Stat. Comput.* **9**(1), 61–79 (1988).
24. J. M. Floryan and H. Rasmussen, Numerical methods for viscous flows with moving boundaries, *Appl. Mech. Rev.* **42**(12), 323–341 (1989).
25. B. J. Daly, Numerical study of two-fluid Rayleigh Taylor instability, *Phys. Fluids* **10**, 297–307 (1967).
26. W. Shyy, H. S. Udaykumar and S.-J. Liang, An interface tracking method applied to morphological evolution during phase change, *Int. J. Heat Mass Transfer* **36**(7), 1833–1834 (1993).
27. W. Shyy, S.-J. Liang and D. Y. Wei, Effect of dynamic perturbation and contact condition on edge-defined fibre growth characteristics. *Int. J. Heat Mass Transfer* **37**, 977–987 (1994).
28. J. M. Sullivan and H. Hao, Comparison of simulated dendritic tip characteristics to those experimentally observed in unconfined environments, *ASME* **HTD234**, 14–19 (1993).
29. Y. Saito, G. Goldbeck-Wood and H. Muller-Krumbhaar, Numerical simulation of dendritic growth, *Phys. Rev. A* **38**(4), 2148–2157 (1988).
30. A. J. DeGregoria and L. W. Schwartz, Finger breakup in Hele–Shaw cells, *Phys. Fluids* **28**(8), 2313–2314 (1985).
31. A. J. DeGregoria and L. W. Schwartz, A boundary

integral method for two-phase displacement in Hele–Shaw cells, *J. Fluid Mech.* **164,** 383–400 (1986).
32. S. O. Unverdi and G. Tryggvason, A front-tracking method for viscous, incompressible multi-fluid flows, *J. Comp. Phys.* **100,** 25–37 (1992).
33. L. N. Brush and R. F. Sekerka, A numerical study of a two-dimensional crystal growth forms in the presence of anisotropic growth kinetics, *J. Crystal Growth* **96,** 419–441 (1989).
34. C. W. Hirt and B. D. Nichols, Volume of fluid (VOF) method for the dynamics of free boundaries, *J. Comp. Phys.* **39,** 201–225 (1981).
35. N. Ashgriz and J. Y. Poo, FLAIR: flux line-segment model for advection and interface reconstruction, *J. Comp. Phys.* **93,** 449–468 (1991).
36. D. B. Kothe and R. C. Mjolsness, RIPPLE: a new method for incompressible flows with free surfaces, *AIAA J.* **30**(11), 2694–2700 (1992).
37. J. A. Sethian and J. Strain, Crystal growth and dendritic solidification, *J. Comp. Phys.* **98**(2), 231–253 (1992).
38. R. Kobayashi, Modeling and numerical simulations of dendritic crystal growth, *Physica D* **63,** 410–423 (1993).
39. A. A. Wheeler, B. T. Murray and R. J. Schaefer, Computations of dendrites using a phase field model, *Physica D* **66,** 243–262 (1993).
40. S. V. Patankar, *Numerical Heat Transfer and Fluid Flow.* Hemisphere, Washington, DC (1980).
41. J. C. T. Wang and G. F. Widhopf, A high-resolution TVD finite volume scheme for the Euler equations in conservation form, *J. Comp. Phys.* **84,** 145–173 (1989).
42. H. Miyata, Finite difference simulation of breaking waves, *J. Comp. Phys.* **65,** 179–214 (1986).
43. K. Morinishi, A finite difference solution of the Euler equations on body-fitted Cartesian grids, *Comput. Fluids* **21**(3), 331–344 (1992).
44. J. J. Quirk, An alternative to unstructured grids for computing gas dynamic flows around arbitrarily complex two-dimensional bodies, ICASE Report No. 92-7, NASA Langley Research Center, Hampton, VA (1992).
45. J. Crank, *Free and Moving Boundary Problems.* Oxford University Press, Oxford (1984).
46. D. Bensimon and P. Pelce, Tip-splitting solutions to the Stefan problem, *Phys. Rev. A* **33,** 4477–4478 ff. (1986).
47. Y. Couder, N. Gerard and M. Rabaud, Narrow fingers in the Saffman–Taylor instability, *Phys. Rev. A* **34**(6), 5175–5178 (1986).
48. H. S. Udaykumar, W. Shyy and M. M. Rao, ELAFINT: a mixed Eulerian–Lagrangian method for fluid flow with complex and moving boundaries, AIAA Paper No. 94-1996 (1994).